Imaging apoptosis: Blankenberg and Strauss provide an overview of recent advances in the molecular imaging of programmed cell death, with a focus on pathophysiology and currently available radiotracers . . . . . ***Page 1659***

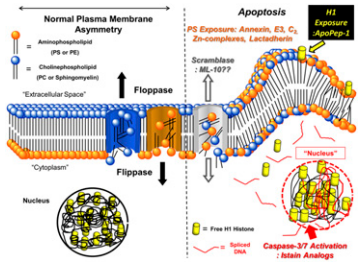

Radioembolization after PRRT: Ezziddin and colleagues report on a study of the safety of ^{90}Y microsphere radioembolization as salvage treatment in patients with neuroendocrine tumors after failed peptide receptor radionuclide therapy . . . . . ***Page 1663***

Bone scans and sunitinib response: Saylor and colleagues evaluate images from a phase 2 study of sunitinib in prostate cancer to assess the significance of tyrosine kinase inhibitor–induced improvements in ^{99m}Tc-MDP bone scans . . . . . ***Page 1670***

Sex-dependent prognosis and SUV_{max}: Wainer and colleagues examine the predictive value of ^{18}F-FDG maximum standardized uptake on PET in a surgical cohort of men and women with surgically treated early non–small cell lung cancer . . . . . ***Page 1676***

PET in suspected NETs: Haug and colleagues investigate the use of ^{68}Ga-DOTATATE PET/CT as a tool for early diagnosis and reliable exclusion in patients with suspected nonlocalized neuroendocrine tumors . . . . ***Page 1686***

Lymphoscintigraphy and nonsentinel node metastasis: Lee and colleagues describe a new model that uses sentinel lymphoscintigraphic findings and histopathologic parameters as covariates for predicting the likelihood of nonsentinel lymph node metastases in breast cancer. . . . . ***Page 1693***

PET index for glioma detection: Kinoshita and colleagues evaluate the utility of ^{18}F-FDG–^{11}C-methionine PET decoupling analysis for quantitatively assessing glioma cell infiltration in nonenhancing MRI T2 hyperintense lesions . . . . . ***Page 1701***

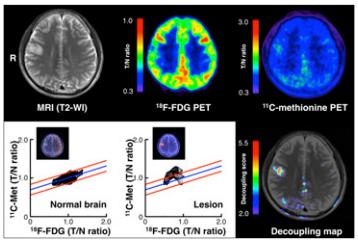

^{11}C-MET PET in gliomas: Singhal and colleagues compare the grading and prognostic value of ^{11}C-methionine PET with that of ^{18}F-FDG PET and contrast-enhanced MRI in patients with gliomas. . . . . ***Page 1709***

Image quality with PSF and TOF PET: Akamatsu and colleagues explore the effects of combined point-spread function and time-of-flight in improving ^{18}F-FDG PET/CT images, with potential for reduced radiation or acquisition times. . . . . ***Page 1716***

Caffeine occupancy of adenosine receptors: Elmenhorst and colleagues describe visualization and quantification of in vivo occupancy of the human cerebral A_1 adenosine receptor using ^{18}F-CPFPX PET. . . . . ***Page 1723***

PET and bony metastases: Chan and colleagues compare the diagnostic accuracy of ^{18}F-FDG PET/CT with that of ^{18}F-fluoride PET/CT in the detection of bony metastases in heightened-risk head and neck cancer patients . . . . . ***Page 1730***

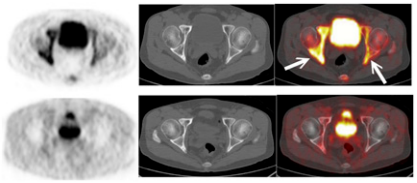

Imaging and liver radioembolization: Uliel and colleagues provide an educational overview of the anatomic, angiographic, and nuclear imaging aspects of endovascular mapping and conjoint ^{99m}Tc-MAA hepatic perfusion imaging before radioembolization with ^{90}Y-loaded microspheres in hepatic malignancies . . . . . ***Page 1736***

Immuno-PET of tissue factor: Hong and colleagues review the development of and initial studies with a PET tracer for imaging of tissue factor expression in pancreatic cancer . . . . . ***Page 1748***

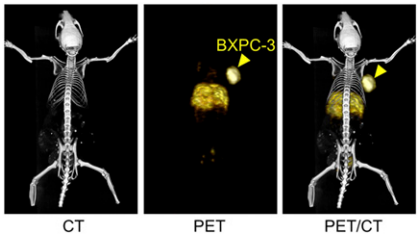

Imaging residual β-cell mass: Gialleonardo and colleagues evaluate uptake mechanisms and retention of the PET tracer ^{11}C-hydroxytryptophan in endocrine and exocrine pancreas in vitro and in vivo . . . . . ***Page 1755***

Antitumor effects of proteasome inhibition: Altmann and colleagues study the effect of the proteasome inhibitor bortezomib on aggressive anaplastic thyroid carcinoma characterized by complete refractoriness to multimodal therapeutic approaches. . . . . ***Page 1764***

^{64}Cu-labeled antibody targeting: Vāvere and colleagues detail the conjugation and biodistribution of a radiolabeled antibody that could facilitate clinical PET assessment of anti-GD2 immunotherapies and complement other imaging modalities in the staging and treatment of neuroblastoma . . . . . ***Page 1772***

^{18}F-FPTP cardiac PET in mice: Kim and colleagues report on initial animal studies with a radiolabeled lipophilic cationic compound with high potential as a mitochondrial voltage sensor for PET imaging . . . . . ***Page 1779***

MuPET camera performance: Wong and colleagues describe a dedicated high-resolution, high-sensitivity, and low-cost preclinical murine PET camera and report on its conformance with NEMA standards . . . . . ***Page 1786***

New class of Aβ tracers: Brockschnieder and colleagues report on a fruitful search for novel chemical entities that can be transformed into ^{18}F-labeled amyloid-β tracers with favorable brain washout kinetics and low background signal for PET imaging . . . . . ***Page 1794***

^{11}C-PHNO whole-body dosimetry: Mizrahi and colleagues measure the whole-body distribution of this promising $D_{2/3}$ agonist for PET imaging, as a function of time in adult subjects to determine the internal radiation dose . . . . . ***Page 1802***

RADAR phantom series: Stabin and colleagues present a new generation of reference computational phantoms for internal and external dosimetry created from image-based models tied to reference masses defined by the International Commission on Radiological Protection. . . . . ***Page 1807***

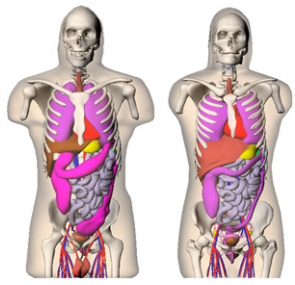

ON THE COVER

In this patient with suspected NET, an intense focus of ^{68}Ga-DOTATATE seen on PET, without abnormalities on CT, was histologically confirmed to be a <10-mm glucagonoma.

See page 1690.